

Superconducting Atomic Contacts under Microwave Irradiation

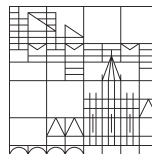
Doctor's Thesis

by

Oliver Aschenbrenner

at the

Universität
Konstanz



Faculty of Science
Department of Physics

1. Reviewer: Prof. Dr. Elke Scheer
2. Reviewer: Prof. Dr. Juan Carlos Cuevas

Konstanz, 2026

Zusammenfassung

Hier könnte Ihre Zusammenfassung stehen.

Abstract

Please insert abstract here.

Kleines Statement¹

Hineinfließen
in die Formen,
die sich stellen.
Sich aber nicht
formen lassen
und auf keinen Fall
erhärteten.

Das wäre
Leben
für mich.

¹Kristiane Allert-Wybranietz (*1955)

Table of Contents

1	Introduction	1
2	Foundations of Superconducting Transport	2
2.1	Superconductivity and Quasiparticles	2
2.1.1	BCS Ground State and Excitations	2
2.1.2	Density of States and the Dynes Parameter	2
2.2	Quasiparticle Tunneling in SIS Junctions	4
2.2.1	Tunnel Current Formula	4
2.2.2	Temperature and Magnetic-Field Dependence	4
2.2.3	Concept of Photon-Assisted Tunneling	5
2.3	(Multiple) Andreev Reflection	6
2.3.1	Andreev Reflection at a Normal-Superconductor Interface	6
2.3.2	Multiple Andreev Reflection in Superconducting Point Contacts	8
2.3.3	Transmission Channels and the Landauer Picture	8
2.4	The Josephson Effect	8
2.4.1	DC Josephson Relation	8
2.4.2	AC Josephson Effect and Shapiro Steps	8
2.4.3	Coherent vs Incoherent Tunneling under Microwaves	8
2.5	Photon-Assisted Tunneling: The Tien-Gordon Model	8
2.5.1	Voltage Modulation and Energy Sidebands	8
2.5.2	Applicability and Limitations	8
2.5.3	Comparison to AC Josephson Effect	8
2.6	Experimental Principles and Measurement Techniques	8
2.6.1	Mechanically Controllable Break Junction (MCBJ)	8
2.6.2	Microwave Coupling and Calibration	8
2.6.3	Measurement Scheme	8
2.7	Summary	8
3	Tunnel-barrier junctions	9
3.1	Dynes DOS, tunneling current	9
3.2	TienGordon photon-assisted tunneling	9
3.3	Suppression by temperature & magnetic field	9
3.4	Asymmetric IV behavior near resonance	9

4 Few-channel atomic contacts	10
4.1 Concept of Quantum Channels in Superconducting Atomic Contacts	10
4.2 Reproduction of Scheer et al. Measurement (your highlight)	10
4.3 Photon-Assisted Multiple Andreev Reflection (PAMAR)	10
4.4 Discussion	11
5 Experimental Methods	12
5.1 Sample Preparation	12
5.1.1 Concept	13
5.1.2 Design	14
5.1.3 Realization	17
5.2 Setup	26
5.2.1 cryostat and thermometer	26
5.2.2 MCBJ	26
5.2.3 DC Cabling	26
5.2.4 AC cabling	27
5.3 Data Acquisition	27
5.3.1 DC Measurement Concept	27
5.3.2 Measurement Software	28
5.3.3 Measurement Script	28
5.3.4 Evaluation Script	28
6 Conclusion	29
7 Appendix	i
7.1 Drivers	i
7.1.1 p5 control	i
7.1.2 GUI	i
7.1.3 Femtos	i
7.1.4 ADwin	i
7.1.5 Bluefors Software	i
7.1.6 Magnet	i
7.1.7 Motor	i
7.1.8 VNA	i
7.1.9 Yoko	i
7.1.10 Keysight	i
7.2 Test	i
References	v

Introduction

Foundations of Superconducting Transport

2.1 Superconductivity and Quasiparticles

2.1.1 BCS Ground State and Excitations

The microscopic description of superconductivity is provided by the Bardeen-Cooper-Schrieffer (BCS) theory, which assumes that electrons near the Fermi surface form bound pairs of opposite momentum and spin (Cooper pairs). The mean-field BCS Hamiltonian reads

$$H_{\text{BCS}} = \sum_{k,\sigma} \xi_k c_{k\sigma}^\dagger c_{k\sigma} - \sum_k (\Delta c_{k\uparrow}^\dagger c_{-k\downarrow}^\dagger + \Delta^* c_{-k\downarrow} c_{k\uparrow}), \quad (1)$$

where $\xi_k = \epsilon_k - \mu$ is the single-particle energy measured from the Fermi level and Δ denotes the superconducting order parameter. Diagonalization via the Bogoliubov transformation yields quasiparticle excitations with energy

$$E_k = \sqrt{\xi_k^2 + |\Delta|^2}, \quad (2)$$

and coherence factors

$$u_k^2 = \frac{1}{2} \left(1 + \frac{\xi_k}{E_k} \right), \quad v_k^2 = \frac{1}{2} \left(1 - \frac{\xi_k}{E_k} \right). \quad (3)$$

The superconducting energy gap Δ depends on temperature and vanishes at the critical temperature T_c . Within the weak-coupling limit this dependence is approximately

$$\Delta(T) \approx \Delta_0 \tanh \left[1.74 \sqrt{\frac{T_c}{T} - 1} \right], \quad (4)$$

where $\Delta_0 \simeq 1.76 k_B T_c$ is the zero-temperature gap.

2.1.2 Density of States and the Dynes Parameter

The excitation spectrum derived above leads directly to a characteristic energy dependence of the quasiparticle density of states (DOS). Within the BCS model,

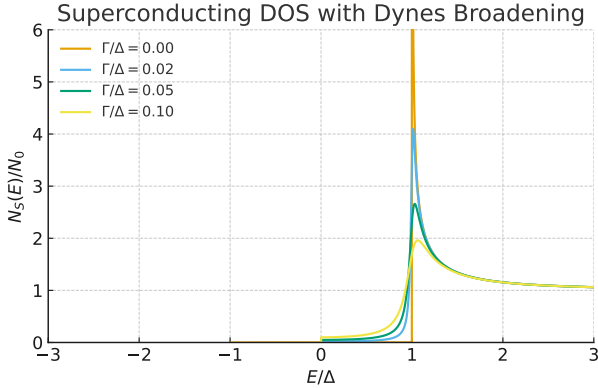


Figure 1 Superconducting density of states $N_S(E)$ with Dynes broadening for $\Gamma/\Delta \in \{0.00, 0.02, 0.05, 0.10\}$.

the normalized superconducting DOS is given by

$$\frac{N_S(E)}{N_0} = \text{Re} \left[\frac{|E|}{\sqrt{E^2 - \Delta^2}} \right], \quad (5)$$

where N_0 is the normal-state DOS at the Fermi level. This expression diverges at the gap edges $E = \pm\Delta$, producing the well-known coherence peaks, and vanishes for $|E| < \Delta$, reflecting the absence of single-particle states inside the energy gap.

In real materials the coherence peaks are broadened due to inelastic scattering, finite quasiparticle lifetimes, and inhomogeneities. A convenient phenomenological description was introduced by Dynes [1], who replaced $E \rightarrow E + i\Gamma$ in the BCS expression. The resulting DOS reads

$$\frac{N_S(E)}{N_0} = \text{Re} \left[\frac{E + i\Gamma}{\sqrt{(E + i\Gamma)^2 - \Delta^2}} \right], \quad (6)$$

where Γ is the socalled Dynes parameter. Increasing Γ smears the singularities and introduces a small finite DOS inside the gap. The parameter is thus a useful measure of the effective quasiparticle broadening or dissipation present in an experiment. Figure 1 illustrates the effect of different Γ/Δ ratios on the shape of the superconducting DOS.

2.2 Quasiparticle Tunneling in SIS Junctions

2.2.1 Tunnel Current Formula

The tunneling current in a superconducting junction can be calculated within the framework of first-order perturbation theory, where the insulating barrier is sufficiently thick to suppress coherent Cooper-pair tunneling. In this limit, the transport is dominated by single-particle tunneling processes. The resulting current through an S-I-S junction is given by the convolution of the densities of states of both electrodes, weighted by the difference of their FermiDirac occupation probabilities,

$$I(V) \propto \int_{-\infty}^{+\infty} N_S(E) N_S(E + eV) [f(E) - f(E + eV)] dE, \quad (7)$$

where $N_S(E)$ is the superconducting density of states and $f(E)$ denotes the Fermi distribution. At zero temperature, current can only flow when filled states in one electrode overlap with empty states in the other. Because no quasiparticle states exist within the energy gap, $|E| < \Delta$, the integral vanishes for $|eV| < 2\Delta$, resulting in a suppressed current around zero bias. Once the applied voltage exceeds $|eV| = 2\Delta$, quasiparticle states begin to overlap, and the current rises steeply. The corresponding differential conductance exhibits sharp coherence peaks at the threshold voltage, directly reflecting the singularities of the superconducting DOS.

At higher bias ($|eV| \gg 2\Delta$), the current approaches the normal-state behavior and scales linearly with V . Finite temperature, inelastic scattering, or lifetime broadening (represented by the Dynes parameter Γ) lead to a rounding of the coherence peaks and a small residual subgap conductance. This model forms the theoretical foundation for the analysis of the experimental I - V characteristics presented in Chapter ??.

2.2.2 Temperature and Magnetic-Field Dependence

The superconducting energy gap Δ is not a fixed quantity but depends sensitively on both temperature and magnetic field. Within the BCS framework, $\Delta(T)$ decreases monotonically with increasing temperature and vanishes at the critical temperature T_c . The temperature dependence can be approximated by the weak-coupling relation

$$\Delta(T) \approx \Delta_0 \tanh \left[1.74 \sqrt{\frac{T_c}{T} - 1} \right], \quad (8)$$

which reproduces the experimentally observed behavior for many conventional superconductors. As the temperature approaches T_c , thermal excitations break

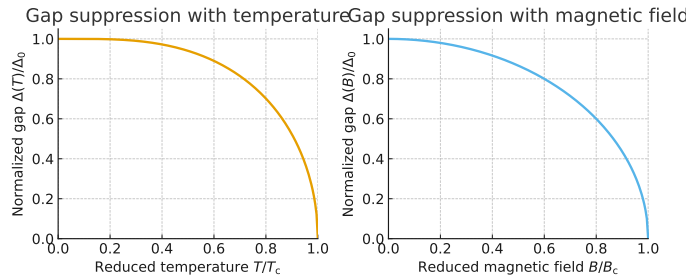


Figure 2 Schematic suppression of the superconducting energy gap Δ with temperature and magnetic field. Left: BCS-like temperature dependence $\Delta(T)/\Delta_0$. Right: phenomenological field dependence $\Delta(B)/\Delta_0 = \sqrt{1 - (B/B_c)^2}$.

Cooper pairs, reducing the superfluid density and leading to a continuous closure of the energy gap.

A similar suppression of the superconducting gap occurs under the influence of an external magnetic field. When a field is applied, screening currents generate pair-breaking effects through orbital motion and Zeeman splitting of the electron spins. In a simple phenomenological description, the field dependence of the gap can be expressed as

$$\Delta(B) = \Delta_0 \sqrt{1 - (B/B_c)^2}, \quad (9)$$

where B_c is the thermodynamic critical field at which superconductivity is destroyed. For thin films or nanostructures, the relevant pair-breaking field can differ from the bulk value due to geometry, disorder, and spinorbit coupling.

Figure 2 schematically illustrates both dependencies, highlighting the continuous closure of the superconducting gap with increasing temperature or magnetic field. These relations are essential for interpreting experimental I - V curves and for distinguishing intrinsic quasiparticle effects from thermal or magnetic suppression of superconductivity.

2.2.3 Concept of Photon-Assisted Tunneling

When a superconducting tunnel junction is exposed to microwave radiation, the time-dependent voltage across the barrier can be expressed as

$$V(t) = V_{dc} + V_{ac} \cos(\omega t), \quad (10)$$

where V_{ac} and ω denote the amplitude and angular frequency of the oscillating field, respectively. The oscillatory potential periodically modulates the phase of the electron wavefunction, allowing tunneling processes that involve the absorption or emission of discrete photon energies $n\hbar\omega$.

Within the framework of Tien and Gordon [2], the total tunneling current under irradiation can be written as a sum over photon-assisted sidebands,

$$I(V_{dc}) = \sum_{n=-\infty}^{+\infty} J_n^2(\alpha) I_0\left(V_{dc} + \frac{n\hbar\omega}{e}\right), \quad (11)$$

where $I_0(V)$ is the unirradiated (dark) current-voltage characteristic, $J_n(\alpha)$ are Bessel functions of the first kind, and $\alpha = eV_{ac}/\hbar\omega$ is the dimensionless microwave amplitude. The term with index n corresponds to tunneling processes involving the absorption ($n > 0$) or emission ($n < 0$) of $|n|$ photons.

This formalism predicts that the current-voltage curve under microwave irradiation is a weighted superposition of shifted replicas of the unperturbed I - V curve, leading to characteristic satellite peaks in the differential conductance at voltages $V_n = V_{dc} + n\hbar\omega/e$. For a superconducting tunnel junction, these sidebands appear symmetrically around the coherence peaks.

The Tien–Gordon model provides a simple yet powerful description of photon-assisted tunneling in the incoherent regime, where the ac field acts as a classical voltage modulation. Its quantitative application to the aluminum tunnel-barrier junctions studied in this work is discussed in Chapter ??.

2.3 (Multiple) Andreev Reflection

this is a placeholder

2.3.1 Andreev Reflection at a Normal-Superconductor Interface

At the interface between a normal metal (N) and a superconductor (S), the continuity of the quasiparticle wavefunction imposes a unique boundary condition on charge transport. When an electron in the normal metal approaches the interface with an energy smaller than the superconducting energy gap ($|E| < \Delta$), it cannot enter the superconductor as a single quasiparticle because no available states exist within the gap. Instead, the electron is reflected as a hole with opposite momentum and spin, while a Cooper pair carrying charge $2e$ is transmitted into the superconductor. This process, known as *Andreev reflection*, ensures charge and momentum conservation across the interface.

In the simplest picture, the incident electron and the reflected hole are phase-correlated; they form the two components of a time-reversed pair. The amplitude of Andreev reflection depends on the transparency of the interface and is maximal for a perfectly clean contact. For a barrier of finite strength, normal reflection competes with Andreev reflection, reducing the probability of Cooper-pair transfer.

This retroreflection mechanism gives rise to a finite conductance at subgap voltages, even when quasiparticle tunneling is forbidden. The probability of Andreev reflection can be derived from the Bogoliubov–de Gennes equations and depends on both the excitation energy and the interface transparency. Andreev reflection is thus the fundamental process linking normal-metal transport to superconducting correlations.

Figure 3 schematically illustrates the process: an electron incident from the normal metal (blue arrow) is reflected as a hole (orange arrow), while a Cooper pair (green arrow) enters the superconductor. This two-particle conversion process underlies many phenomena discussed later in this thesis, such as multiple Andreev reflection and Josephson transport in atomic-scale contacts.

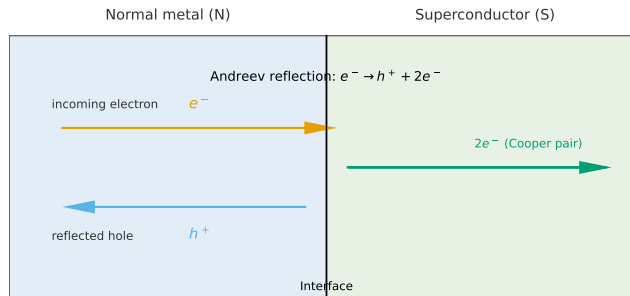


Figure 3 Schematic illustration of Andreev reflection at a normal-superconductor interface. An incoming electron from the normal metal (blue arrow) is reflected as a hole (orange arrow), while a Cooper pair (green arrow) is transmitted into the superconductor.

2.3.2 Multiple Andreev Reflection in Superconducting Point Contacts

2.3.3 Transmission Channels and the Landauer Picture

2.4 The Josephson Effect

2.4.1 DC Josephson Relation

2.4.2 AC Josephson Effect and Shapiro Steps

2.4.3 Coherent vs Incoherent Tunneling under Microwaves

2.5 Photon-Assisted Tunneling: The Tien-Gordon Model

2.5.1 Voltage Modulation and Energy Sidebands

2.5.2 Applicability and Limitations

2.5 Experimental Principles and Measurement Techniques

2.6.1 Mechanically Controllable Break Junction (MCBJ)

2.6.2 Microwave Coupling and Calibration

2.6.3 Measurement Scheme

2.7 Summary

Table 1 Overview of key theoretical concepts and where they are applied in the thesis.

Concept	Later Chapter	Physical Regime
Dynes DOS + Tien-Gordon	Ch. ??	Tunnel-barrier junctions
FCS + MAR	Ch. ??	Few-channel contacts
Incoherent pair tunneling	Ch. ??	High-transmission regime

Tunnel-barrier junctions

Chapter 3: Tunnel-barrier junctions (Al AlO_x Al)

Short theory section: -

3.1 Dynes DOS, tunneling current

formula (BCS + Dynes broadening). -

3.2 Tien–Gordon photon-assisted tunneling

- . - Suppression of I_c under irradiation (qualitative Josephson discussion).
Results/discussion: - IV curves under irradiation Tien-Gordon fits extraction of T_e . -

3.3 Suppression by temperature & magnetic field

- . -

3.4 Asymmetric IV behavior near resonance

(speculative discussion).

Purpose: demonstrate that you can quantitatively explain behavior in the low-transmission limit.

Few-channel atomic contacts

Chapter 4 Few-Channel Atomic Contacts

4.1

4.1 Concept of Quantum Channels in Superconducting Atomic Contacts

- Short recap of Landauer formula and transmission eigenchannels. - Introduce pincode terminology and cite Scheer et al. (1997). - Explain why determining the transmission distribution is crucial for interpreting MAR and microwave effects.

4.2

4.2 Reproduction of Scheer et al. Measurement (your highlight)

- Describe your breaking-trace measurement and fitting routine. - Show several I-V traces during elongation and extracted transmission vectors. - Compare to canonical results emphasize that this validates your setup. - Discuss possible deviations (temperature, noise, fitting uncertainty).

4.3

4.3 Photon-Assisted Multiple Andreev Reflection (PAMAR)

- Build on the established pincode and show how microwaves modify those MAR features. - Present simulations (FCS + modified Tien-Gordon).

4.4

4.4 Discussion

- Comment on consistency between pincode, MAR behavior, and microwave response.

Chapter 4: Few-channel atomic contacts (intermediate transmission)

Short theory section: - Full Counting Statistics (FCS) for MAR including AC drive. - Modified Tien-Gordon for finite transmission. - Mention that JC is neglected in simulation (justify).

Results/discussion: - MCBJ conductance evolution channel pin-code (compare to Elke Scheer). - PAMAR structures and their microwave modulation. - Agreement between experiment and FCS-based simulation.

Purpose: connect microscopic channel picture to measurable photon-assisted MAR signatures.

Experimental Methods

In this chapter, I will describe the experimental methods used in this work.

First, I will discuss the sample preparation process. Although the fabrication of break junctions is well-established within the group, significant changes have been made to the design. These improvements have led to the development of a new protocol, enhancing the overall quality and stability of the samples.

The second section covers the physical setup. Considerable time was invested in making modifications, performing routine maintenance, and addressing issues with aging components. In particular, the cabling for direct current (DC) and alternating current (AC) measurements underwent significant upgrades to improve reliability and performance.

In the third section, I will describe the electronics used. This includes an overview of the general setup and a detailed discussion of the newly implemented measurement program. Additional technical details about the Python implementation can be found in the appendix. Finally, I will present the measurement and evaluation protocols, including the data processing methods.

5.1 Sample Preparation

Single-electron transistors (SETs) consist of two junctions forming a small island, which is capacitively coupled to a DC gate electrode. Typically, this configuration is achieved using two oxide barriers in a lead, fabricated through shadow evaporation [3, 4, 5].

In our approach, however, one oxide barrier is replaced by a mechanically controlled break junction (MCBJ). Aluminum is chosen as the material due to its superconducting properties at low temperatures [6, 7, 8]. Additionally, an AC gate or strip line is incorporated to ensure efficient and controlled coupling of microwave fields.

This section describes work conducted together with Patrick Raif as part of his project practical¹ [9].

The following subsections detail the sample preparation process from various perspectives. First, the conceptual framework is outlined. Next, I delve into

¹A component of the master's curriculum completed within a semester.

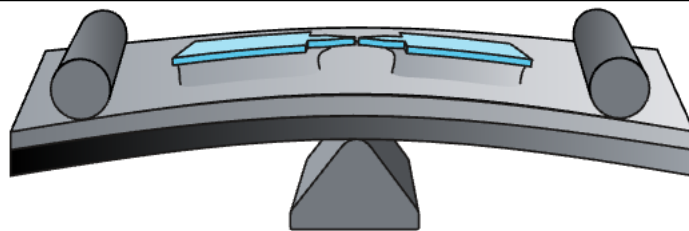


Figure 4 Here comes some text

the design choices and the rationale behind the procedural decisions. Finally, I present a step-by-step guide to the process, sharing practical tips and addressing challenges encountered in the laboratory.

5.1.1 Concept

In this subsection, I explain the general concept of the sample preparation process and its connection to the underlying physics.

A MCBJ is implemented using a freestanding bridge-like structure on a bendable substrate. Figure 1 illustrates a schematic of the MCBJ used in this work. The substrate can be bent either by pushing a stamp from below or by pressing counter rods from above. This bending action elongates the freestanding bridge, enabling the MCBJ to form atomic contacts.

The physical setup of the MCBJ is described in more detail in Subsection 5.2.2.

A polyimide (PI) layer insulates the substrate from the structures produced in the subsequent steps. More importantly, the PI layer serves as a sacrificial layer. During later processing, it is partially etched, allowing the structure to become freestanding.

Next, two layers of positive electron-sensitive resist are applied. Electron beam lithography (EBL) is then used for precise exposure. After development, the exposed resist is dissolved, leaving the desired pattern.

For the SET, beside the MCBJ, a second weak link is formed by creating an oxide barrier. A convenient approach for this is shadow evaporation, also known as the Niemeyer-Dolan technique [10, 11]. This process involves two evaporation steps performed at different incident angles, which slightly offset the structure in each step. Between these steps, a controlled oxidation process can be performed without breaking the vacuum. This creates overlapping areas with a metal-oxide-metal cross-section, as illustrated in Figure 5.

Since a superconducting single-electron transistor (SSET) is planned, aluminum (Al) is selected for both evaporation steps. This results in an Al break

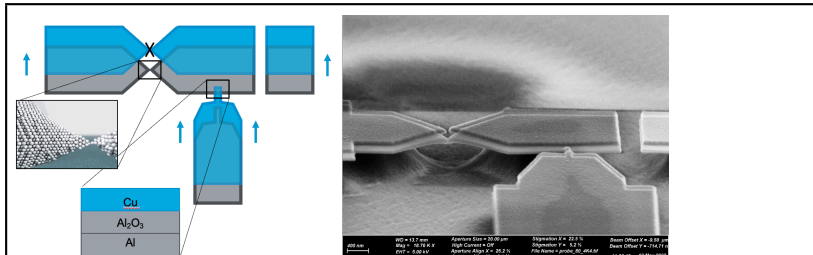


Figure 5 Here comes some text

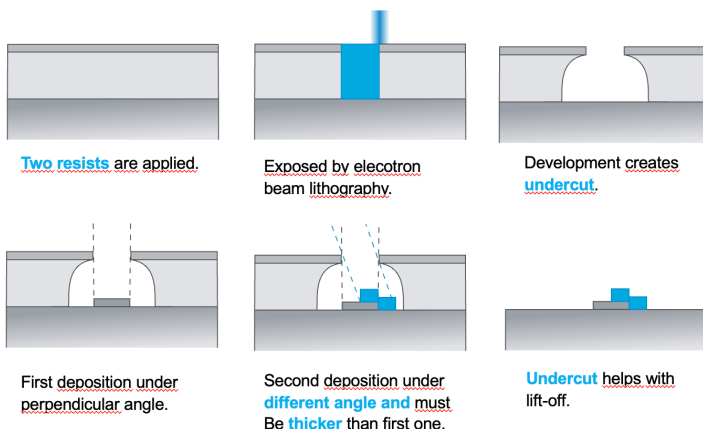


Figure 6 Here comes some text

junction (BJ) and an Al-Al₂O₃-Al oxide barrier, as described Thomas Lorenz [6] and Susanne Sprenger [7]. Alternatively, the second material can be different; for instance, Al-Al₂O₃-Cu has been successfully realized by Laura Sobral Rey [8].

As the final step, approximately 500 nm of the polyimide (PI) layer is etched using oxygen plasma. The homogeneous etching process creates a significant undercut, as illustrated in Figure 5. This final step renders the break junction freestanding and fully functional.

5.1.2 Design

This subsection explains the sample preparation process in terms of design decisions. While there is no single definitive path to a finished sample, different approaches can have subtle effects. Here, I outline the decision-making process

behind the individual steps.

Bronze has been used as a substrate by many generations of doctoral students in this group. One key reason is that it requires relatively low force to bend while maintaining excellent elastic behavior. This is crucial for MCBJ, where the configuration needs to be adjusted repeatedly. Other materials, such as copper, exhibit less homogeneous bending and tend to deform primarily in the middle, directly beneath the stamp. This leads to a greater change in angle and poorer elastic properties. Additionally, copper often displays non-monotonic bending behavior, making fine adjustments in the atomic contact regime impractical. On the other hand, PI substrates² bend uniformly across their length but fail to achieve sufficient bending for the MCBJ to function effectively. Materials like copper-beryllium, although mechanically suitable, are toxic and therefore unsuitable for use. Another critical requirement is that the substrate material must be non-magnetic and have minimal magnetic impurities. Considering all these factors, bronze has proven to be the most suitable substrate for MCBJ applications over the years. [schirm_uss_2009]

A polyamide (PA) layer is applied by spin-coating onto an entire bronze wafer. Following a hard-baking process, the PA is converted into PI. Subsequently, two layers of resist are applied. The thin top layer, optimized for high-resolution lithography, ensures the resulting structure has sharp and well-defined edges. The thicker bottom layer serves a dual purpose: elevating the top layer and acting as a sacrificial layer that forms an undercut during development. Two mechanisms contribute to the formation of this undercut. First, the bottom layer receives a higher electron dose because electrons diffuse through the resist, and back-scattered electrons further enhance exposure in the bottom layer. Second, an extended time in isopropyl alcohol (IPA) after development with diluted methyl isobutyl ketone (MIBK) amplifies the undercut effect.

EBL is performed using a Zeiss Crossbeam system, which has been modified to achieve significantly faster beam blanking. The beam blander operates in synchronization with the beam deflection, allowing precise exposure of any desired structure within the specified field of view. Typically, a 100μm field is used for small, high-resolution structures, while a 1000μm field is employed for coarser, larger features. For structures exceeding these field sizes, the sample stage can be moved to enable exposure of multiple adjacent fields. To ensure seamless transitions between fields, an overlap is planned to facilitate stitching of the different areas.

At the start of my doctoral studies, only one of the two available EBL programs, Elphy Plus by Raith, was functional and properly supported. As a result, I had to implement the new sample design from scratch. The dimensions of the break junction (BJ) and gate are consistent with those shown in Figure 7 and as previously implemented by References [6, 7, 8]. In contrast, the design of the finger forming the oxide barrier was modified to be thicker towards its lower part.

²PI substrates are also called Kapton.

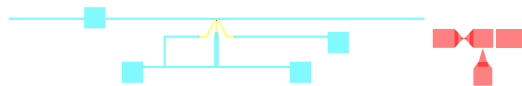


Figure 7 blablabla.

This adjustment reduces the freestanding length of the evaporation mask, thereby increasing its stability. However, an issue arose with older resist material, which tends to sag during evaporation. Consequently, the finger does not reliably reach the island during the second evaporation step, leading to potential inconsistencies in the structure.

The larger leads and pads are arranged and optimized to facilitate easy electrical contacting. An AC gate or stripline is included at an 8 μ m distance to ensure maximum microwave irradiation. Its length is maximized while maintaining a reasonable writing time during electron beam lithography. Additionally, a shorting structure is integrated into the design to protect the sensitive tunnel barrier from static discharge. The central vertical lead is made thicker to enhance its contrast, which aids in precisely aligning the BJ with the stamp during setup.

The evaporator used in this work features a long distance between the evaporation source and the sample. This setup results in aluminum being evaporated in a highly directional manner but also significantly reduces the effective cross-section of the deposition. The evaporator provides two methods for aluminum deposition: thermal evaporation and electron beam evaporation. In thermal evaporation, a large current heats a small crucible, causing the aluminum to evaporate. However, the crucible used for thermal evaporation is delicate and must be loaded and run empty after each use to avoid crack formation. This process is tedious, prone to errors, and offers no significant advantages over electron beam evaporation. In electron beam evaporation, a focused electron beam heats the aluminum crucible locally, allowing for a more efficient and reliable

deposition process. Therefore, in contrast to References [6, 7, 8], electron beam evaporation was used in this work.

The oxidation step between the two evaporation processes is carried out in the load lock of the evaporator at a low oxygen pressure of approximately 3.0(2) mbar for 3 minutes [8]. In the past, this step was inconsistent and difficult to reproduce. As a result, it is now closely monitored to ensure reliability [7, 12].

Reactive ion etching (RIE) is performed using the *PlasmaPro 80 ICP RIE system* from Oxford Instruments. Although this machine is not originally designed for homogeneous etching, acceptable uniformity can be achieved by operating it with low table radio frequency (RF) power, high inductively coupled plasma (ICP) RF power, and high chamber pressure. The ICP system generates a high-density plasma by coupling energy into the chamber via an electromagnetic field, while the RF power applied to the table controls the ion energy impacting the sample surface. A heated table further enhances the homogeneity of the etching process. The etched depth is monitored in real-time using laser interferometry, ensuring precise control over the process.

The final step is contacting the sample. Wedge bonding is unsuitable for this purpose because the bonding wire can press through the pad into the soft PI layer. Instead, thin copper wires are attached to the pads using conductive silver paste. This method ensures reliable electrical contact without damaging the underlying structure.

5.1.3 Realization

This subsection serves as a practical guide, outlining the small but critical steps necessary for successful sample preparation.

Wafer Preparation

Start with a 300 µm thick bronze wafer, which is typically covered by a protective foil. To remove the foil without damaging the wafer, cool the wafer in liquid nitrogen and then gently peel off the shards. This method is both effective and non-destructive. The next step is to polish the wafer. Attach a polishing head made from sewn cotton cloth to a drill. Use aluminum oxide particles in the form of a white compound block as the abrasive material. The polishing head should be adequately moistened, preferably soaked, with a solvent such as alcohol or IPA, as these have proven effective. Secure the wafer to a smooth, milled steel block using double-sided adhesive tape³. Ensure that no tape protrudes from beneath the wafer to avoid interference during polishing. Begin polishing by moving the polishing head from top to bottom. This approach prevents debris generated during the process from settling back onto the wafer, which would

³e.g. Tesa Universal

require additional polishing to remove. Rotate the steel block periodically, as it is easier to polish the lower section of the wafer. Polishing is complete when the wafer achieves a uniform mirror-like finish across its surface. To detach the wafer from the steel block, cool it again in liquid nitrogen. For cleaning, rinse the wafer sequentially with acetone and then IPA, ensuring the acetone is removed completely before using IPA. Finally, dry the wafer with pressurized nitrogen gas while the IPA is still wet to avoid leaving any residues behind. [13]

Another option for polishing involves using sandpaper with progressively finer grit on a glass slide, as described by Patrick Raif [14]. However, this method has been omitted due to its significantly higher time requirements, despite its superior ability to minimize long-range surface variations.

Next, prepare the spin coater, PA, and vacuum oven. The PA is pre-portioned into small crimp-seal vials to minimize moisture exposure and ensure faster warming. Retrieve one vial from the freezer and allow it to reach room temperature while preheating the convection oven to 135 °C. Line the interior of the spin coater with aluminum foil and ensure the vacuum oven is operational, with its chamber open.

To remove any adsorbed water from the wafer, place it on a hot plate at 100 °C for at least one minute. For proper adhesion to the 1 in-chuck, apply a layer of parafilm, ensuring it is securely bent around the chuck's edges. Create five small holes in the parafilm using a syringe— one at the center and one near the edge in each cardinal direction. Allow the wafer to cool to room temperature before centering it on the chuck. Once centered, activate the vacuum pump. Before applying the PA, test the spin-coating program to confirm proper adhesion. This step is especially critical for larger wafers, as adhesion issues may not be readily apparent due to limited use.

Blow the wafer with nitrogen to remove any residual dust. Pour the PA onto the wafer, ensuring it covers approximately 90% of the surface and avoiding air bubbles. If bubbles are present, gently pop or move them using a syringe, being careful not to scratch the wafer. Start the spin-coating process with an initial spread cycle at 300 rpm for 30 s, followed by a final spin at 5000 rpm for 90 s. Transfer the wafer directly to the convection oven for a 5 min soft bake at 135 °C. For hard baking, use the vacuum oven with a programmed cycle that ramps up to 400, °C, holds for 30, min, and then cools to room temperature over several hours. Detailed instructions and the temperature profile for the vacuum oven can be found in Reference [14]. Baking immediately after spin coating has been shown to improve results.

The application of resists A4 and EL11 follows a similar process. Aluminum foil is unnecessary, as these resists can be easily cleaned with acetone. Ensure the resists are not expired, as prolonged storage significantly affects their performance. Further details are provided in the Appendix in Table 3.

The wafer is now ready to be cut into smaller pieces measuring 3 ×, 8 mm. This is done using a custom-made shear sheet cutter equipped with spacers of 3 mm and 18 mm. Before using the cutter, clean the cutting edges thoroughly

with IPA to ensure precise and contamination-free cuts. Samples taken from the wafer's edges are more likely to have variations in the thickness profiles of the PI and resists. For consistent and reliable sample fabrication, it is recommended to use pieces from the center of the wafer, where the resist layers are more uniform. Thickness variations at the edge may impact the required electron beam dose during lithography. Once the samples are cut, place them in a chip tray⁴ for safe handling and storage.

Electron beam lithography

The next step involves performing EBL using the Crossbeam system. Begin by utilizing the jug with a Faraday cup to measure the beam current. To locate the Faraday cup efficiently, you can use a position list in the Zeiss software. Ensure that the working distance is as close as possible to 5.00 mm for optimal results. Note that the beam current may not stabilize immediately, so it's advisable to wait for some time or return later to perform the measurements.

Aligning the sample horizontally is critical for accurate exposure. The Focused Ion Beam (FIB) toolbox provides alignment tools that simplify this process. Zoom out to the maximum view and use the upper-right corner of the sample and the farthest left edge for initial alignment. This method is sufficient for correcting angular misalignment. While you can further refine alignment using features in the Elphy Plus software, it is unlikely to improve the angle alignment once the sample is mounted in the cryostat.

Next, focus the beam in the upper-right corner of the sample. Use the wobbling tool to position the beam in the center of the aperture, and reduce astigmatism using the stigmator adjustments for both the *x*- and *y*-axes. Once the beam is well-focused, check the beam current at the Faraday cup. For the 30 µm aperture in high-current mode, the beam current should be approximately 0.5 nA. This aperture setting is critical for small and precise structures. For the 120 µm aperture, which is used for the 1000 µm writing fields, the beam current is less critical since the bigger leads are more tolerant of under-exposure. In fact, under-exposing larger fields can reduce writing time without compromising quality. The beam current for the 120 µm aperture in high-current mode should typically be around 5 nA. Perform a final focusing step at the central position of the upper edge of the sample. Look for a dirt particle on the resist to aid in focusing, and confirm that the working distance remains at 5.00(1) mm. At this stage, also ensure that the beam shift is set to zero.

Before initiating the writing process, note the current time. The design layout includes a timestamp, which can help you correlate your notes with the physical sample. If the measured beam current deviates from previous settings, recalculate the settling time for the 100 µm field accordingly. The executed position list in the Elphy Plus software will automatically locate the writing fields, apply the

⁴e.g. Entegris

corresponding settings and write the design.

Repeat the whole alignment, focus and writing process for the next samples until you have a batch size of 4-5 samples.

If it has been several weeks since your last EBL session, it is recommended to check the alignment between the 100 μm and 1000 μm fields before writing your first sample. To do this, expose a 100 μm field and one surrounding 1000 μm field in the upper-right corner of the sample. The exposed resist will differ in appearance from the unexposed areas, allowing you to assess alignment accuracy. Be mindful that prolonged observation can unintentionally expose the resist, reducing contrast and making the alignment harder to judge. If misalignment is detected, adjust the settings accordingly. For instance, if the 100 μm field is shifted left, adjust U by $-\Delta X$; if shifted upward, adjust V by $-\Delta Y$. Repeat this process as needed until the alignment is satisfactory.

Once the EBL is complete, the samples must be developed. Begin by preparing the necessary solutions: fill a crimp-seal vial with a mixture of one part MIBK to three parts IPA. Additionally, prepare separate crimp-seal vials containing pure IPA— one for each sample being developed.

To develop the sample, immerse it in the MIBK/IPA solution for 25 s, gently swirling the vial throughout this duration to ensure uniform exposure. After 25 s, promptly transfer the sample into a vial with pure IPA and continue swirling. Note that the MIBK/IPA solution can be reused for all samples in the same batch, but fresh IPA should be used for each individual sample to maintain cleanliness. Leave the sample in the IPA solution for 60 s before removing it. Once removed, dry the sample carefully with a stream of nitrogen gas. Throughout the process, securely hold the sample with tweezers to avoid unnecessary handling or accidental release during the waiting or transfer steps. Finally, inspect the developed samples under a light microscope to confirm that the patterns have been developed successfully and are free of defects.

Shadow Evaporation

To begin the shadow evaporation process, place the sample holder on a hot plate set to 100 °C for a few minutes. This step helps to remove any adsorbed water, significantly improving the vacuum quality. Verify the orientation of the sample to ensure the shadow evaporation proceeds in the correct direction. For optimal results, load the sample into the load lock and leave it under vacuum overnight or longer. This extended pumping period further enhances the vacuum quality.

When ready, transfer the sample holder into the main chamber for the first evaporation. Using electron beam evaporation, deposit 60 nm of aluminum at an angle of 4°. Take care to heat the crucible gradually over 5-10 min to prevent damage to the crucible and ensure uniform evaporation. Ensure the crucible is sufficiently filled with aluminum; typically, adding 1-3 pellets per evaporation is sufficient.

After completing the first evaporation, transfer the sample back to the load lock and close the pumping line. Introduce pure oxygen into the load lock to achieve a pressure of 3.0(2) mbar and allow the sample to oxidize for 3 minutes. To terminate the oxidation process, reopen the pumping line. To achieve a sufficient vacuum level of approximately 10^{-6} mbar, ensure the oxygen feeding line is thoroughly evacuated.

Once the load lock vacuum is restored, transfer the sample back into the main chamber for the second evaporation. Deposit 100 nm of aluminum at an angle of 34° to complete the shadow evaporation process.

To ensure the formation of a well-oxidized Al_2O_3 layer, it is essential to achieve a smooth aluminum surface. However, during the process, I encountered the formation of numerous dimples. Despite trying several approaches to minimize them, no definitive solution emerged. It appears that higher evaporation rates, specifically above 4 Å/s, tend to result in fewer dimples, though the difference is not statistically significant. Contrary to previous recommendations, a less deep vacuum or a shorter time interval between the last vacuum break and evaporation seemed to favor a reduction in the number of dimples. One might question the extended focus on achieving a high-quality vacuum in the load lock. The working theory behind this approach is that it prevents the sample from evaporating water or other contaminants during the aluminum deposition. While a poor vacuum in the main chamber may encourage nucleation around contaminants, potentially leading to a smoother surface, the observed effects were not significant enough to draw definitive conclusions, and further investigations were not pursued.

The lift-off process is carried out by placing the sample in a crimp-seal vial filled with pure acetone. Heat the vial on a hot plate at approximately 60°C for 1-3 h. After this, use a pipette to carefully agitate the acetone inside the vial, ensuring that all metal flakes are removed. Rinse the sample with IPA and then blow it dry with nitrogen to complete the process.

Plasma Etching

As penultimate step, etching the samples using the PlasmaPro 80 ICP RIE by Oxford is performed. Although this tool is not designed for homogeneous etching, it can be adapted to achieve this by operating at low table RF and high pressures. To stabilize the plasma before entering a less stable condition that favors homogeneous etching, an ignition step is implemented. The temperature is critical in achieving the desired undercut. A temperature of 100°C has proven to be optimal, as it provides a sufficient undercut while maintaining a slow enough process to control the etching depth. However, the parameter I found after some optimization, can be found in Table 2.

A laser interferometer is used to monitor the etching depth. For optimal exposure, find a spot on the sample, avoiding metal structures, where the reflected intensity is as high as possible, but not saturated. During etching, the inten-

Table 2 RIE reciprocating MCBJ SSET v5 @ 100C

Parameter	Stabilization	Ignition	Etching
Process time	5 min	5 s	30 min
Table heater	100 °C	-	-
Oxygen flow	50 sccm	-	-
Pressure	100 mTorr	ramp	250 mTorr
<hr/>			
Table RF			
Power Demand	-	20(5) W	3(5) W
Max Reflected Power	-	5 W	2 W
Tolerance Time	-	7 s	-
Min DC Bias	-	1 V	-
AMU (C1, C2)	-	(41 %, 23 %)	-
<hr/>			
ICP RF			
Power Demand	-	400(50) W	-
Max Reflected Power	-	100 W	-
Tolerance Time	-	10 s	-
AMU (C1, C2)	-	(64 %, 39 %)	-

sity follows a cosine curve, which, although imperfect, is still recognizable. The number of periods m you need to wait depends on the laser wavelength λ , the desired depth d , and the refractive index $n = 1.81$ [15]. For our process, we typically optimize for

$$m = \frac{2 \cdot n \cdot d}{\lambda} = \frac{2 \cdot 1.81 \cdot 500 \text{ nm}}{632.8 \text{ nm}} = 2.86 \quad (12)$$

periods. An example curve of the laser intensity over time is shown in Figure 8.

Since the etching speed varies significantly between samples, it is recommended to etch each sample individually for optimal results.

Contacting

Contacting the sample was initially a challenging task for me, and it took gathering advice from many current and former users. Eventually, I realized that the main issue was shaky hands. Shakiness can be caused by factors such as caffeine, caffeine deprivation, lack of sleep, stress, and poor eyesight. To address this, I stopped drinking coffee, as I realized I am quite sensitive to it. To reduce stress, I also made it a point not to contact more than one sample per day. I took my time, and if I wasn't feeling up to it, I would postpone the task until the

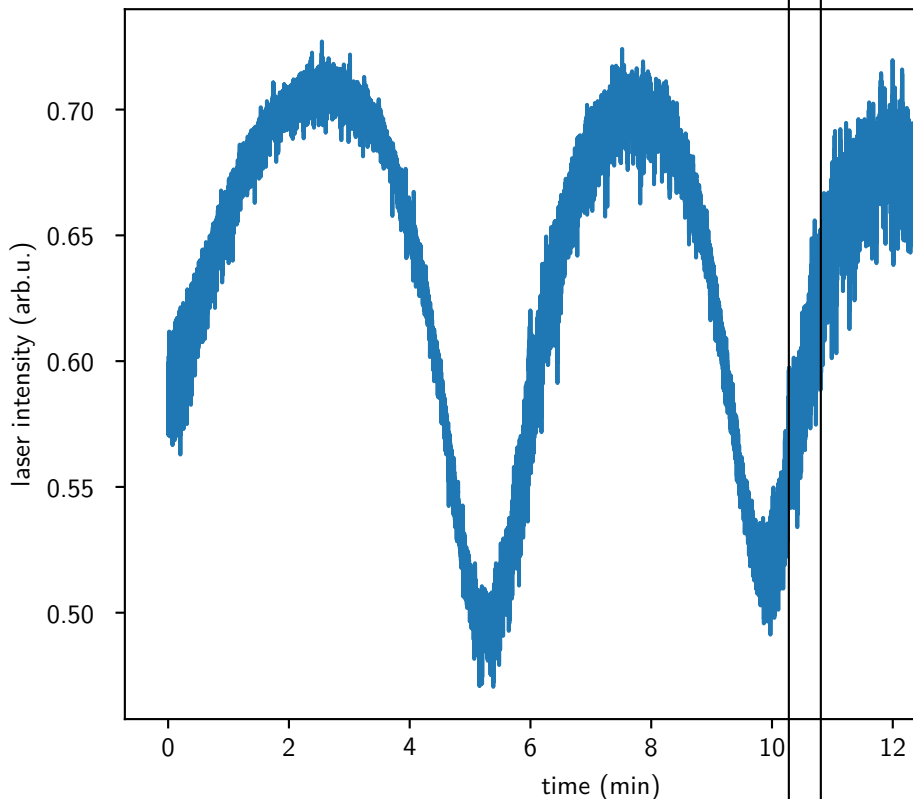


Figure 8 Laser intensity during etch process

next day. After all the previous production steps, losing samples due to rushed contacting is far more costly than taking the time to do it right.

As for my eyesight, I discovered that I am nearsighted, which is not so bad, but I also have astigmatism, which makes things more challenging. The poor lighting around the workbench made it even worse. I found that working at the workbench in the middle of P5 offered two advantages over other spots: good lighting options and a relatively high table. This allowed me to maintain a comfortable position while being close to the sample, even when sitting on a low chair.

To fixate the sample, I use adhesive strips⁵ on a copper plate, which allows some movement of the plate but keeps the sample fixed in place. The next step is to prepare some insulated copper wires soldered to post connectors. You should strip the insulation off the wire tips, and the bias lines can be twisted. It's important to keep the wires as short as possible—4–5 cm is usually enough. Be sure to insulate the rear part of the post connector with an insulating varnish⁶.

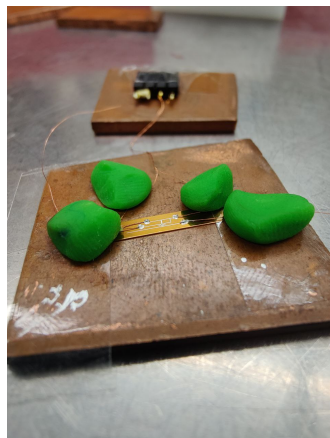
Position the wire tips with the help of play dough so that they touch the pads of the sample. Then, using a sharpened toothpick, apply a small amount of silver paste onto the wire and pad. Make sure to use silver paste specifically for contacting, as its viscosity is critical for a proper connection. The paste should be just enough to wet the sample so that only the pad is connected. If the viscosity is too low, it could cause a short circuit; too high, and the wire will stick to the toothpick instead of the pad. To prevent this, use the silver paste in the lid after shaking the paste bottle, and just cover the tip of the toothpick.

Next, use two-component epoxy to provide strain relief for the wires. The viscosity of the epoxy is crucial here as well. If you use the epoxy too soon after mixing, it will continue to flow and could touch unwanted areas. The interaction between the epoxy and silver paste is not fully understood, so it's important to avoid mixing them. I typically test the epoxy by making small test dots and waiting for the right consistency before applying it. Each side should be glued separately, as the working time is narrow.

After loading the sample into the cryostat, the final step is to scratch the shortage with an engraving tool. During this process, and while closing the radiation shields, ensure that you are properly grounded by wearing a grounding bracelet. It is also recommended, to do this task barefoot and to raise the humidity with an air humidifier to prevent static buildup.

Table 3 here goes some text.

Sacrificial layer	Durimide 115A
Spinning	spread cycle: 300 rpm for 30 s spin cycle: 5000 rpm for 90 s ramps for 3 s, Program 3
Soft baking	135 °C for 5 min in convection oven
Hard baking	400 °C for 30 min in vacuum oven
Spacing layer	MMA(8.5)MAA EL11
Spinning	spread cycle: 500 rpm for 5 s spin cycle: 2500 rpm for 90 s ramps for 3 s, Program 1
Soft baking	150 °C for 1 min on hot plate
Electron resist	950 PMMA A4
Spinning	spread cycle: 500 rpm for 5 s spin cycle: 5000 rpm for 60 s ramps for 3 s, Program 2
Hard baking	170 °C for 30 min in convection oven
Exposure	Crossbeam by Zeiss, Elphy Plus by Raith
Settings	10 kV acceleration, 5 mm working distance,
Aperture	30 µm and 100 µm aperture, high current, 155 µC/cm ² area dose
Development	25 s in 1 MIBK + 3 IPA 60 s in IPA
Shadow Evaporation	First layer: 60 nm Al at -4 ° Oxidation: 3 mbar of O ₂ for 3 min Second layer: 100 nm Al at 34 °
Lift-off	1 h in acetone at 60 °C
Reactive Ion Etching	PlasmaPro 80 ICP RIE by Oxford MCBJ SSET v5 @ 100C, see Table 2

Figure 9 blabla

Parameter for Sample Preparation

5.2 Setup

5.2.1 cryostat and thermometer

5.2.2 MCBJ

Danke Martin!

5.2.3 DC Cabling

4point measurements

⁵e.g. tesafilm® standard by Tesa

⁶e.g. GE Low Temperature Varnish (59-C5-101) by Oxford Instruments

copper powder filter

steel capillary cable

silver epoxy filter

5.2.4 AC cabling

Attenuators

Antenna

stripline

5.3 Data Acquisition

In this section i want to focus on the used electronics. I scheme the measurement principle and the work on grounding. I'll also talk about the self-developed measurement program and go through the written drivers. A great deal of developing is done by Florian Kayatz, within his Hiwi (cite: Flo). Finally I will also talk about the data treatment and processing.

5.3.1 DC Measurement Concept

As mentioned in Subsection 5.2.3 a 4-point measurement principle is used. Given, by the former described setup, tiny voltages should be measurable. Instead an analog to digital converter ADwin Gold 2, in combination with two femto preamplifier, is used.

Previously for SSET experiments at the Scheer2 cryostat a combination of NF, SRT and a similar ADC (by NI) was used by References [6, 7, 8]. On the Bluefors a combination of Femto amplifier and Keysight multimeter was used by Reference [16].

All combinations of DAC Keysight1, Keysight2 and Adwin Gold 2 with Preamplifiers Femto, NF und SRT has been tested, regarding the electrical noise. I found, that the combination of ADwin Gold 2 and Femto preamplifier provided the lowest noise floor. This combination offers some further advantages. The Femto pre-amplifiers has a high bandwidth and still works analog opposite to SRT pre-amplifier. Also, it can be remote controlled, what is super beneficial, when operating with a script or not on-sight for different amplification settings. The Femto amplifier can be operated with 4 different amplifications: 10, 100, 1000, 10000. The DAC measures continuously, with high bandwidth and on two channels simultaneously in opposition of the Keysight multimeters. All this, helps

to correlate the two measured channels with each other in order to reliably measure I-V curves.

As a source, the function generator, used by References [6, 7, 8], KeysightB, used by [16] and the DAC of the already used ADwin. Again, the usage of ADwin was best for the lowest noise floor. However, to enhance the resolution, part of the - layout - AD converter - Pre Amplifier

5.3.2 Measurement Software

- P5 control - devices in appendix

5.3.3 Measurement Script

- explain iv_script_v2.py - test

5.3.4 Evaluation Script

- binning - data treatment

Conclusion

Appendix

7.1 Drivers

into the appendix

7.1.1 p5 control

7.1.2 GUI

7.1.3 Femtos

7.1.4 ADwin

7.1.5 Bluefors Software

7.1.6 Magnet

7.1.7 Motor

7.1.8 VNA

7.1.9 Yoko

7.1.10 Keysight

7.2 Test

Reference [17]

307.28986pt4.25279in 4.25279in 107.99876mm 107.99876mm

Figure 10

Figure 11

Program 1

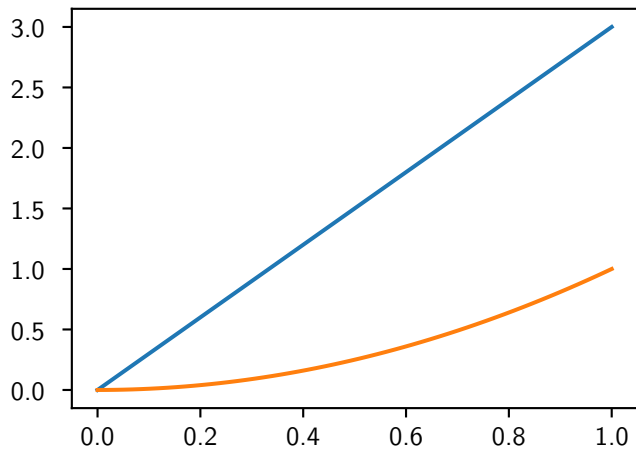


Figure 10 Complex susceptibility

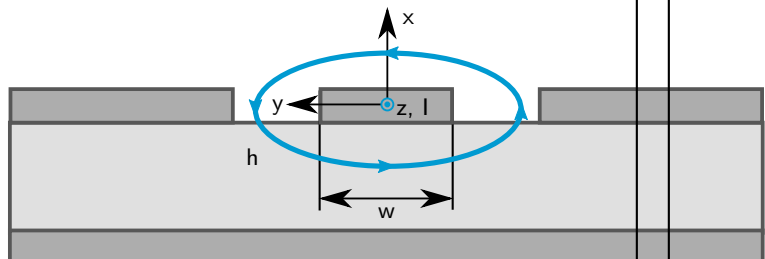


Figure 11 blablabla.

Program 1 Listing Caption is above.

```
1 """version from 15.12.23
2 author: Oliver Irtenkau
3
4 features: Corporate Design Colors of University Konstanz
5 and inverse colors for more contrast
6
7 """
8
9 import numpy as np
10 import matplotlib.pyplot as plt
11
12 x = np.linspace(0, 1, 1001)
13 y = 3 * x
14 plt.plot(x, y)
15 plt.plot(x, x**2)
```

Option 1 No explicit Miscellaneous chapter

This is the cleanest for most theses. You integrate every bit of content under one of the main scientific chapters or the appendices. Use appendices for anything that is: technical but not central (calibration curves, fitting scripts, additional IV traces), background or validation measurements (e.g., temperature calibration, microwave attenuation tests).

Then the main text stays focused and logical.

Option 2 A short Miscellaneous Results chapter

If you have several small, independent results that dont warrant full chapters for example: supplementary microwave experiments (different frequencies, powers), tests on non-AI samples, noise measurements, comparisons between fitting methods,

then you can group them as a compact Additional Experiments and Analysis or Miscellaneous chapter near the end.

Suggested layout:

Chapter 6 Additional Experiments and Analyses

6.1 Temperature and Magnetic-Field Dependence Briefly show confirmation that the devices behave as expected (e.g. gap suppression).

6.2 Frequency-Dependent Effects Show the asymmetric IV features and discuss possible causes (resonances, heating, impedance mismatch).

6.3 Auxiliary Measurements and Calibrations Include details such as microwave coupling, line attenuation, or base-temperature determination.

Keep this concise it shouldnt look like an afterthought but rather a supporting evidence collection.

Option 3 Miscellaneous Appendices

If your miscellaneous content is highly technical or data-heavy: Appendix A: Detailed fitting procedure for TienGordon model Appendix B: Raw IV data and error estimation Appendix C: Microwave calibration Appendix D: Temperature extraction via Dynes fits

That keeps your main story crisp but documents everything transparently.

Recommendation for you

Given your description so far, I'd suggest: No Miscellaneous chapter in the main thesis body. Instead, include a short Additional Experiments section at the end of your High-Transmission chapter (for asymmetric IVs etc.), and move purely technical or validation content to appendices.

That way, everything still feels intentional and thematically grouped.

References

- [1] R. C. Dynes, V. Narayanamurti, and J. P. Gorno. "Direct Measurement of Quasiparticle-Lifetime Broadening in a Strong-Coupled Superconductor". In: *Physical Review Letters* 41.21 (Nov. 20, 1978). Publisher: American Physical Society, pp. 1509–1512. DOI: 10.1103/PhysRevLett.41.1509. URL: <https://link.aps.org/doi/10.1103/PhysRevLett.41.1509> (visited on 10/30/2025).
- [2] P. K. Tien and J. P. Gordon. "Multiphoton Process Observed in the Interaction of Microwave Fields with the Tunneling between Superconductor Films". In: *Physical Review* 129.2 (Jan. 15, 1963). Publisher: American Physical Society, pp. 647–651. DOI: 10.1103/PhysRev.129.647. URL: <https://link.aps.org/doi/10.1103/PhysRev.129.647> (visited on 03/13/2025).
- [3] T. A. Fulton and G. J. Dolan. "Observation of single-electron charging effects in small tunnel junctions". In: *Physical Review Letters* 59.1 (July 6, 1987), pp. 109–112. ISSN: 0031-9007. DOI: 10.1103/PhysRevLett.59.109. URL: <https://link.aps.org/doi/10.1103/PhysRevLett.59.109> (visited on 03/13/2025).
- [4] Torsten Henning. *Charging effects in niobium nanostructures*. Jan. 27, 1999. DOI: 10.48550/arXiv.cond-mat/9901308. arXiv: cond-mat/9901308. URL: <http://arxiv.org/abs/cond-mat/9901308> (visited on 03/13/2025).
- [5] V A Krupenin, A B Zorin, D E Presnov, M N Savvateev, and J Niemeyer. "Metallic single-electron transistor without traditional tunnel barriers". In: *Physics-Uspekhi* 44.10 (Oct. 1, 2001), pp. 113–116. ISSN: 1468-4780. DOI: 10.1070/1063-7869/44/10S/S25. URL: <https://iopscience.iop.org/article/10.1070/1063-7869/44/10S/S25> (visited on 03/13/2025).
- [6] Thomas Lorenz. "Wechselspiel von Vierteilchen-Transport und Ladungseffekten in supraleitenden Einzelelektronentransistoren". Doctoral. Konstanz: Konstanz, 2018.
- [7] Susanne Sprenger. "Interplay between charging effects and multi-particle transport in superconducting single electron transistors with tunable junctions". Doctoral. Konstanz: Konstanz, 2019.

- [8] Laura Sobral-Rey. "Interplay between charging effects and multiparticle charge transport processes in a tunable single electron transistor". Doctoral. Konstanz: Konstanz, 2022.
- [9] Patrick Raif. "Electronic Transport through Superconducting Atomic Contacts under Microwave Irradiation". Master. Konstanz: Konstanz, 2024.
- [10] J. Niemeyer and V. Kose. "Observation of large dc supercurrents at nonzero voltages in Josephson tunnel junctions". In: *Applied Physics Letters* 29.6 (Sept. 15, 1976), pp. 380–382. ISSN: 0003-6951, 1077-3118. DOI: 10.1063/1.89094. URL: <https://pubs.aip.org/apl/article/29/6/380/531269/Observation-of-large-dc-supercurrents-at-nonzero> (visited on 03/13/2025).
- [11] G. J. Dolan. "Offset masks for lift-off photoprocessing". In: *Applied Physics Letters* 31.5 (Sept. 1, 1977), pp. 337–339. ISSN: 0003-6951, 1077-3118. DOI: 10.1063/1.89690. URL: <https://pubs.aip.org/apl/article/31/5/337/45825/Offset-masks-for-lift-off-photoprocessing> (visited on 03/13/2025).
- [12] Teo Conzelmann. "Optimierung der Herstellung und elektrische Charakterisierung ultrakleiner Tunnelkontakte aus Aluminium und Aluminiumoxid". Bachelor. Konstanz: Konstanz.
- [13] Erik Oberg and Christopher J. McCauley, eds. *Machinery's handbook: a reference book for the mechanical engineer, designer, manufacturing engineer, draftsman, toolmaker, and machinist*. 26. ed. New York: Industrial Press, 2000. 2630 pp. ISBN: 978-0-8311-2625-4 978-0-8311-2635-3.
- [14] Patrick Raif. "Fabrication of a Superconducting Single-Electron Transistor". Project Practical. Konstanz: Konstanz.
- [15] *Duramide-100 US12*. 2012.
- [16] Martin Prestel. "Magnetic Order in Atomic Contacts of Strong Paramagnets". Doctoral. Konstanz: Konstanz, 2020.
- [17] Lukas Schertel, Oliver Irtenkauf, Christof M. Aegerter, Georg Maret, and Geoffroy J. Aubry. "Magnetic-field effects on one-dimensional Anderson localization of light". In: *Physical Review A* 100.4 (Oct. 14, 2019), p. 043818. ISSN: 2469-9926, 2469-9934. DOI: 10.1103/PhysRevA.100.043818. URL: <https://link.aps.org/doi/10.1103/PhysRevA.100.043818> (visited on 03/13/2025).

Acknowledgement

Dankeschön und so.

Wer das ließt ist schlau. Haha!